Bio-Design and Manufacturing (2024) 7:955–971
https://doi.org/10.1007/s42242-024-00310-5

RESEARCH ARTICLE

Light/pH dual controlled drug release "nanocontainer" alleviates tumor hypoxia for synergistic enhanced chemotherapy, photodynamic therapy and chemodynamic therapy

Shihe Liu[1] · Xin Zhang[1] · Zhimin Bai[1] · Yibo Yang[1] · Jia Zhang[1] · Kun Li[1,2] · Zhiwei Liu[1,2] · Ming Shi[1,2] · Lixin Dong[3] · Jidong Wang[1] · Jian Li[1,4]

Received: 11 August 2023 / Accepted: 2 July 2024 / Published online: 19 October 2024

Abstract

Photodynamic therapy (PDT) has significant advantages in treating primary tumors. However, the hypoxic tumor microenvironment hinders the generation of sufficient reactive oxygen species during PDT to effectively kill tumor cells, further greatly limiting the applications of PDT in cancer treatment. Herein, we reported a temperature/pH dual controlled drug delivery system LPC@PCN@PDA/Fe^{3+}-AS1411 based on a porous coordination network (PCN (Mn)) coated with polydopamine (PDA) and modified with an aptamer AS1411. β-lapachone (LPC) was loaded inside the PCN (Mn) framework, and Fe^{3+} was attached to the surface of the PDA coating. These nanoparticles (NPs) exhibited excellent multimodal cancer therapeutic effects and tumor targeting ability with their photo- and chemodynamic properties. The therapeutic effect can be enhanced by the production of sufficient oxygen by the internal hydrogen peroxide, which improves the photodynamic effect of the photosensitizer PCN (Mn) and the chemotherapy effect of β-lapachone. Notably, the conversion of Fe^{2+} to Fe^{3+} in the tumor cells exerts the Fenton effect, which generates hydroxyl radicals that cause lipid peroxidation in tumor cells and induce apoptosis, thus enhancing the chemodynamic therapeutic effect. In vitro and in vivo experiments revealed that the NPs demonstrated specific tumor targeting, excellent inhibition effect on tumor growth, and biocompatibility. Together, our findings can help develop an intelligent multifunctional therapeutic nanoplatform for cancer therapy.

✉ Jian Li
Lijianbio@ysu.edu.cn

[1] Hebei Key Laboratory of Applied Chemistry, Hebei Key Laboratory of Nanobiotechnology, Hebei Key Laboratory of Heavy Metal Deep-Remediation in Water and Resource Reuse, Yanshan University, Qinhuangdao 066004, China

[2] Qinhuangdao Biopha Biotechnology Co., Ltd., Qinhuangdao 066000, China

[3] The First Hospital of Qinhuangdao, Qinhuangdao 066000, China

[4] Department of Biological Engineering, College of Environment and Chemical Engineering, Yanshan University, Qinhuangdao 066004, China

Graphic abstract

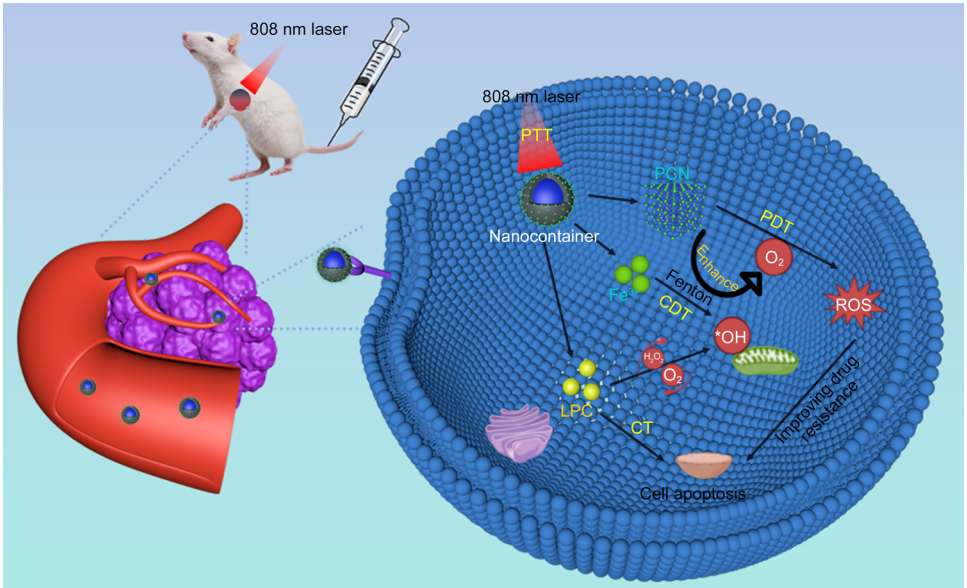

Keywords Porous coordination network (Mn) framework · Phototherapy · Photodynamic therapy · Chemodynamic therapy · Fenton effect

Introduction

In clinical cancer treatment, both chemotherapy and radiation therapy have several limitations, such as chemoresistance, incomplete treatment, and periodic recurrence [1–3]. To overcome these drawbacks, alternative strategies have been developed, including multimodal combination therapy, which can complement other therapies to improve the efficacy of tumor treatment. Photodynamic therapy (PDT), a typical oxidative therapeutic strategy, utilizes a photo-activated photosensitizing agent along with ambient oxygen (O_2) to produce high levels of toxic reactive oxygen species (ROS) for killing cancer cells [4, 5]. Due to its noninvasive nature, PDT provides rapid effect and on-demand controllability, making it advantageous in primary tumor treatment. PDT is effective in several types of tumors and can also overcome drug resistance to enhance the effect of chemotherapy [6].

β-Lapachone (LPC) is a novel chemotherapeutic agent that inhibits tumor cell proliferation via the accumulation of positive DNA superhelix through direct interaction with topoisomerase 1, disrupting DNA replication. Additionally, tumor cells contain higher levels of NAD(P)H:quinone oxidoreductase-1 (NQO1), which can catalyze LPC to produce hydrogen peroxide (H_2O_2) [7]. However, the ability of LPC to produce H_2O_2 depends on the oxygen content within the tumor. Tumor cells consume a large amount of O_2 to facilitate rapid cell proliferation, resulting in a long-term hypoxic microenvironment, which significantly limits the application of PDT and the antitumor effect of LPC [4, 8]. Therefore, improving the tumor's hypoxic environment is a prerequisite to ensure the efficacy of combined treatment using PDT and chemotherapy.

In situ O_2 generation is an effective strategy during tumor therapy to overcome tumor hypoxia. Certain metal ions, including iron and manganese ions, can react with H_2O_2 to produce hydroxyl radicals (OH), which is collectively known as the Fenton effect [9]. Therefore, Fenton or Fenton-like catalysts show satisfactory therapeutic effects against malignant tumors by catalyzing the generation of O_2 and ·OH from H_2O_2, which can alleviate hypoxia while enabling chemodynamic therapy (CDT) [10–12].

Polydopamine (PDA) is a melanin analog with a high photothermal conversion rate (about 40%). It is also pH-sensitive and can be degraded under alkaline conditions [13, 14]. Therefore, we chose PDA as the encapsulation material for the LPC-loaded porous coordination network (Mn) (PCN (Mn)) to avoid leakage of LPC into the blood circulation and achieve acid-responsive release in tumor cells. Moreover, the excellent photothermal properties of PDA promote the complete release of LPC from the PCN organometallic framework while generating local heat for PDT.

Herein, we reported a light/pH-dual-smart responsive nanodrug delivery system, which could effectively improve tumor tissue hypoxia for multimodal combination therapy. LPC was loaded into the PCN (Mn) formed by combining manganese ions and the photosensitizer porphyrin.

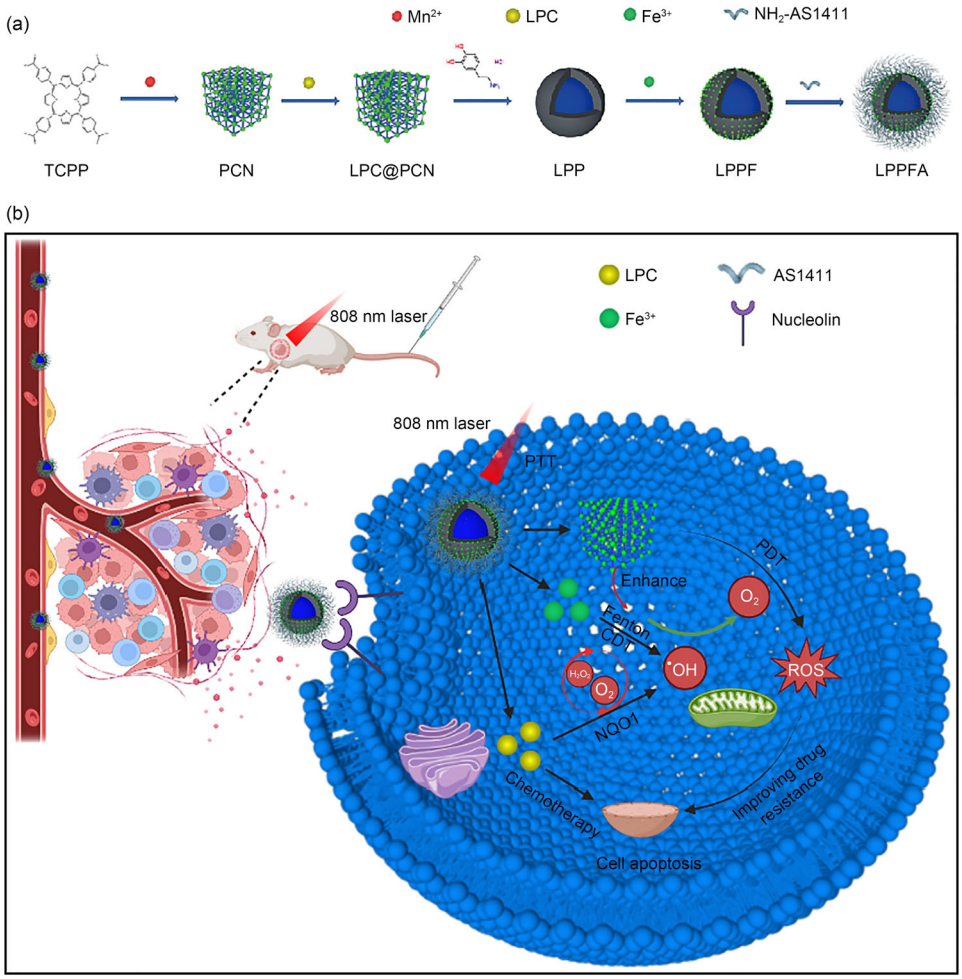

Scheme 1 **a** Schematic diagram of synthesis of the LPPFA smart drug delivery system and **b** diagram of its in vivo antitumor mechanism. LPPFA: LPC@PCN@PDA/Fe^{3+}-AS1411; LPC: β-lapachone; PCN: porous coordination network; PDA: polydopamine; TCPP: tetra(4-carboxyphenyl)porphyrin; LPP: LPC@PCN@PDA; LPPF: LPC@PCN@PDA/Fe^{3+}; PTT: photothermal therapy; CDT: chemodynamic therapy; PDT: photodynamic therapy; ROS: reactive oxygen species; NQO1: NAD(P)H:quinone oxidoreductase-1

Then, PDA was polymerized on the PCN (Mn) surface to prevent drug leakage during transportation. Finally, trivalent iron ion (Fe^{3+}) and a nucleic acid aptamer AS1411 were attached to the PDA surface to develop an intelligent nanodrug delivery system (LPC@PCN@PDA/Fe^{3+}-AS1411 (LPPFA)) with multimodal effect to achieve synergistic enhancement. AS1411 can target the tumor cells and, combined with passive targeting, enable drug accumulation in tumor sites after the nanoparticles (NPs) enter the blood circulation. After entering the tumor cells through endocytosis, PDA in LPPFA undergoes acid degradation to release LPC, porphyrins, and Fe^{3+} ions under acidic conditions inside lysosomes. Then, laser irradiation of porphyrins exerts PDT to reduce LPC resistance and achieve combined PDT and chemical therapy. The Fe^{3+} ions catalyze excess H_2O_2 in tumor cells to produce O_2, enhancing PDT to kill tumor cells effectively. Moreover, H_2O_2 produced using LPC can act as the substrate for the Fenton reaction. In addition, the generated divalent iron (Fe^{2+}) and manganese ion in the PCN (Mn) produce the Fenton effect in the presence of H_2O_2 to further release toxic ·OH. The metal reduction reaction also depletes reduced glutathione (GSH) levels, diminishing the antioxidant capacity of cancer cells. Therefore, the LPPFA NPs with light/pH-controlled release properties could improve the tumor hypoxic environment and disrupt the redox homeostasis of tumor cells to enhance the combined antitumor effect of CDT and PDT (Scheme 1).

Experimental section

Materials

Manganese dichloride tetrahydrate ($MnCl_2{\cdot}4H_2O$), ferric chloride hexahydrate ($FeCl_3{\cdot}6H_2O$), fluorescein isothiocyanate (FITC), and methylene blue (MB) were purchased from Aladdin Chemical Reagent Co., Ltd. (Shanghai, China). Tetra(4-carboxyphenyl)porphyrin (TCPP) was purchased from TCI (Shanghai, China). LPC was obtained from Bide Pharmatech Ltd. (Shanghai, China). Dopamine hydrochloride (DA-HCl) and diphenylbenzofuran (DPBF) were purchased from Sigma-Aldrich (USA). NH_2-AS1411

(5′-NH_2-TTG GTG GTG GTG GTT GTG GTG GTG GTG G-3′) was supplied by Sangon Biotech (Shanghai, China). 4,6-diamino-2-phenylindole (DAPI), cell counting kit-8 (CCK-8), 2′,7′-dichlorodihydrofluorescein diacetate (DCFH-DA), Calcein/PI cell viability/cytotoxicity assay kits, mitochondrial membrane potential assay kits with Rhodamine 123 and Annexin V-FITC apoptosis detection kits were obtained from Beyotime Biotechnology Co., Ltd (Shanghai, China). Dulbecco's modified Eagle's medium (DMEM) and fetal bovine serum (FBS) were purchased from Gibco (New York, USA). Penicillin and streptomycin were purchased from Thermo Science (Beijing, China). Alanine transaminase (ALT), aspartate aminotransferase (AST), blood urea nitrogen (BUN), creatinine (CRE), malondialdehyde (MDA), and glutathione (GSH) assay kits were all obtained from Nanjing Jiancheng Bioengineering Institute (Jiangsu, China). All the chemical reagents were of analytical grade and used without further purification.

Cell lines and experimental animals

The mouse cervical cancer cell line U14 was purchased from Tongpai Biotechnology Co., Ltd. (Shanghai, China). Human lung microvascular endothelial cells (HMVECs) and cervical cancer HeLa cells were obtained from Hongshun Biotechnology Co., Ltd. (Shanghai, China). The U14 cells were passaged in the mouse abdominal cavity, while the HMVECs and HeLa cells were cultured and passaged in a DMEM complete medium (supplemented with 10% FBS, 1% penicillin, and 1% streptomycin). Female Kunming mice ((20 ± 2) g) were purchased from Beijing Vital River Laboratory Animal Technology Co., Ltd. (Beijing, China) and raised under a 12-h-light/-dark cycle specific pathogen free (SPF) environment with a relative humidity of (40 ± 10)% and room temperature of (22 ± 2) °C.

Synthesis of LPPFA

Synthesis of the PCN (Mn) and LPC loading

The PCN (Mn) was synthesized using the solvothermal method [15]. For this, 20 mg each of solid $MnCl_2{\cdot}4H_2O$ and TCPP powders was weighed and dispersed in 20 mL of dimethylacetamide (DMF) solution. After sonicating for 10 min to dissolve completely, the two solutions were mixed. Then, 400 μL of acetic acid was added simultaneously, sonicated for 10 min, and transferred into a 50 mL Teflon reaction-lined hydrothermal reactor. The reaction kettle was sealed and placed in an oven at a temperature of 150 °C. Approximately 12 h later, a black precipitate was obtained, which was further lyophilized to obtain PCN (Mn).

Then, 6 mg of PCN (Mn) and 1 mg of LPC were dissolved in 7 mL of ethanol, mixed well, transferred to a 10 mL centrifuge tube, and fixed on an automatic tumbler with tumbling for 12 h to obtain LPC@PCN.

The encapsulation efficiency (EE) and drug loading (DL) of the LPC in the LPC@PCN were evaluated using ultracentrifugation combined with ultraviolet (UV) spectroscopy. The concentration of nonencapsulated LPC was determined according to the standard curve of LPC ethanol solution concentration versus the optical density (OD) value at 430 nm. Finally, EE and DL of LPC were calculated using the following formulas:

$$\mathrm{EE} = \frac{W_\mathrm{g} - W_\mathrm{u}}{W_\mathrm{g}} \times 100\%, \tag{1}$$

$$\mathrm{DL} = \frac{W_\mathrm{g} - W_\mathrm{u}}{W_\mathrm{gn}} \times 100\%, \tag{2}$$

where W_g, W_u, and W_gn denote the gross drug mass, nonencapsulated drug mass in the supernatant solution, and the gross mass of the LPC@PCN, respectively.

Synthesis and surface modification of LPC@PCN@PDA

Next, DA was polymerized on the surface of LPC@PCN using an amide reaction to form the PDA coating. After dissolving 20 mg of solid LPC@PCN powder in 17 mL of Tris–HCl buffer solution (pH = 10, 0.05 mmol/L), 20 mg of DA-HCl solid powder was added and stirred for 10 min. Then, 3 mL of isopropanol was slowly added as the blocking agent, and the reaction was performed for 6 h. Finally, the PCN (Mn) with PDA coating LPC@PCN@PDA (LPP) was obtained using high-speed centrifugation (13,000 r/min, 10 min).

To further chelate Fe^{3+} on the LPP, 40 mg of solid LPP powder and 20 mg of solid $FeCl_3{\cdot}6H_2O$ were dissolved in 20 mL of ultrapure water, stirred using a magnetic stirrer for 6 h at room temperature, and centrifuged to obtain chelated Fe^{3+} modified LPP NPs, known as LPC@PCN@PDA/Fe^{3+} (LPPF) NPs.

As PDA contains active C=C double bonds that can react with several groups, such as –NH_2 and –SH, NH_2-AS1411 can be added to LPPF by amide reaction [16]. For this, 19 mg of LPPF NPs were weighed and dispersed in 5 mL of Tris–HCl buffer solution (pH = 10, 0.05 mmol/L), transferred to a 10 mL centrifuge tube along with 30 μg/mL of NH_2-AS1411, and incubated for 24 h at room temperature. The mixture was centrifuged to derive the final product, LPC@PCN@PDA/Fe^{3+}-AS1411 (LPPFA).

Characterization of materials

The size and morphology of the samples were observed by transmission electron microscopy (TEM, HT-7700, Hitachi, Japan). Dynamic light scattering (DLS) was used to evaluate the size distribution and zeta potential of the NPs (Malvern Nano ZS90, Morven Instruments Ltd., UK). The UV–Vis absorption spectra of the samples were measured by a UV–Vis spectrophotometer (UV-2550, Shimadzu Co., Ltd., Japan). The metal elemental contents were analyzed by scanning electron microscope (SEM, S-4800, Hitachi, Japan). AS1411 was analyzed using agarose gel electrophoresis with a gel imaging system (Omega fluor plus, Aplegen Inc., USA).

Photothermal property assay of LPPFA in vitro

The in vitro photothermal performance of LPPFA was evaluated by irradiating either 1 mg/mL or different concentrations of LPPFA using a fixed power setting of 2 W/cm^2 or different powers of the 808 nm near-infrared (NIR) laser for 10 min. The solution temperatures were recorded every 30 s, and the time–temperature curves were photographed with an infrared thermal imager and plotted. To further evaluate the photothermal stability of LPPFA NPs, 1 mg/mL of LPPFA was irradiated with four consecutive "on/off" 808 nm NIR laser irradiation cycles, and the temperature of the solution was monitored every 30 s using a digital thermometer.

Determination of drug release in vitro

The ability of PDA to be degraded under acidic conditions and photothermally converted under irradiation with an 808 nm NIR laser irradiation further promotes the diffusion of small molecule drugs from PCN (Mn). The drug release performance of LPPFA was determined by changing the pH (phosphate buffer saline (PBS) buffer, pH = 7.4 or pH = 5.0) of the dialysate with/without irradiation (808 nm NIR, 2 W/cm^2). The LPPFA solution was divided into four parts (1 mg/mL each) and added to dialysis bags, which were then placed in PBS with magnetic stirring at 37 °C for dialysis at either pH = 7 or pH = 5 with or without 808 nm NIR laser irradiation. Every hour, 1 mL of the dialysate was collected and its concentration was determined using the LPC standard curve. The LPC release rate was calculated using Eq. (3) and plotted on the LPC release curve.

$$\text{LPC release} = \frac{W_r}{W_t} \times 100\%, \tag{3}$$

where W_t and W_r denote the mass of the total loaded and released drug, respectively, in the dialysate.

In vitro photodynamic performance evaluation

The samples of each group ((1) H_2O (110 μL), (2) H_2O_2 (10 μL) + H_2O (100 μL), (3) H_2O_2 (10 μL) + LPC@PCN@PDA/AS1411 (LPPA; 100 μL), and (4) H_2O_2 (10 μL) + LPPFA (100 μL)) were added into a centrifuge tube containing 2 mL of ethanol solution of DPBF at a concentration of 100 μg/mL. These samples were irradiated with a 660 nm laser (50 mW/cm^2, 10 min) and the UV absorption of DPBF solution at 417 nm was measured 6 times every 5 min. The changes in absorbance of DPBF with different treatments were recorded and plotted.

Hemolysis

For the hemolysis experiment, 5 mL of blood was drawn from the inferior wing vein of chickens and transferred into a centrifuge tube containing the anticoagulant ethylenediaminetetraacetic acid (EDTA) Na_2. After mixing gently by turning up and down, the sample was centrifuged (1000 r/min, 5 min) to obtain the red blood cells (RBCs). LPPFA NPs dissolved in normal saline at concentrations of 31.25, 62.5, 125, 250, 500, and 1000 μg/mL were mixed with the RBCs, incubated at 37 °C for 30 min, and centrifuged at 2000 r/min for 10 min. Distilled water and normal saline were used as positive and negative controls, respectively. Finally, 200 μL of the supernatant was placed in a 96-well plate in three parallel groups each, and the absorbance of the samples was detected at 570 nm using a multimode microplate reader (Varioskan LUX, Thermo Scientific, USA). The hemolysis rates of NPs were calculated according to Eq. (4):

$$\text{Hemolysis} = \frac{OD_{570s} - OD_{570nc}}{OD_{570pc} - OD_{570nc}} \times 100\%, \tag{4}$$

where OD_{570s}, OD_{570pc}, and OD_{570nc} denote the absorbances of different concentrations of LPPFA-treated samples, positive control (distilled water), and negative control (normal saline), respectively.

Cellular uptake and localization of LPPFA

Before the experiment, the PDA on the LPPF and LPPFA NPs was labeled using FITC [17]. Then, the cells were plated in a 24-well plate and were cultured, reaching a 60% fusion rate. PBS, LPPF (1 mg/mL), or LPPFA nanoparticles (1 mg/mL) were added and co-incubated with the cells for 12 h. After the cells were washed with PBS 2–3 times, the nuclei were stained with DAPI for 10 min. The cells were observed and photographed using a fluorescence microscope (DM4B, Leica, Germany). The fluorescence intensity of FITC in HeLa cells was quantified using flow cytometry (FCS) (FACSCalibur, Becton, Dickinson & Co., USA).

Intracellular ROS, MDA, and GSH content detection

Intracellular ROS production was detected using the fluorescent probe DCFH-DA kit [18]. The cells were seeded in a 24-well plate, and when the cell fusion rate reached approximately 50%, PBS, LPC, PCN@PDA/AS1411 (PPA), LPPA, and LPPFA were added to each group, and three parallels were set for each group. The cells were incubated in a CO_2 incubator for 12 h to promote drug uptake. Then, after irradiating the PPA, LPPA, and LPPFA treatment groups using a 660 nm NIR laser, DAPI was added to the cells and incubated for 10 min. The diluted DCFH-DA was added and incubated in the CO_2 incubator at 37 °C for 20 min. The intracellular ROS production in cells was observed under a fluorescent microscope (DM4B, Leica, Germany). The levels of MDA and GSH in cells and tumor tissues of different treatment groups were measured according to the instructions on the MDA and GSH kits.

Evaluation of cytotoxicity, mitochondrial membrane potential, and cell apoptosis

We evaluated the cytotoxicity and proliferation inhibition of the nanocarrier PCN@PDA and different formulas (PBS, PPA, LPC, LPPA + 808 nm, LPPFA + 808 nm, LPPF + 808 nm + 660 nm, LPPFA + 808 nm + 660 nm) on HMVECs and HeLa cells line using the CCK-8 assay. One day after seeding the cells in a 96-well plate (5×10^4 cells/well), when the cell fusion rate was about 50%, the nanocarrier and different formulas were added and incubated for 12 h. The cells were either left untreated or irradiated with an 880 nm NIR (2 W/cm^2) or/and 660 nm NIR (50 mW/cm^2) laser for 5 min. After incubating the cells in the CCK-8 solution for 1 h, the absorbance of the cells at 450 nm was measured by a multimode microplate reader (Varioskan LUX, Thermo Scientific, USA). The cell viability was calculated based on the following equation:

$$\text{Cell viability} = \text{ODs}/\text{ODc} \times 100\%, \tag{5}$$

where ODs was the mean absorbance at wavelength of 450 nm in the different tested groups and ODc was the mean absorbance at wavelength of 450 nm in the PBS control group.

As the mitochondrial membrane potential decreases during the early stages of cellular apoptosis [19], we detected the changes in the mitochondrial membrane potential caused by LPPFA using a mitochondrial membrane potential assay kit (Rhodamine 123). As Rhodamine 123 only enters the mitochondria of living cells, the significant decrease in the intensity of yellow–green fluorescence in the mitochondria indicates apoptosis or necrosis. Cells treated with PBS, LPC, LPPFA + 808 nm, and LPPFA + 808 nm + 660 nm were incubated for 12 h. Then, after incubating the cells in 250 μL of Rhodamine 123 staining solution for 20–60 min in a CO_2 incubator, the staining solution was replaced with DAPI to stain the nuclei. The cells were observed and photographed under a fluorescence microscope (DM4B, Leica, Germany).

To further investigate whether LPPFA treatment can induce cell apoptosis, FCS was performed after Annexin V-FITC/PI double staining. Cells treated with PBS, LPC, LPPFA + 808 nm, and LPPFA + 808 nm + 660 nm were digested with trypsin and transferred into centrifuge tubes. After centrifugation (1000 r/min, 5 min), 200 μL of Annexin V-FITC and 10 μL of PI staining solution were added to cells sequentially. Then, FCS was performed to evaluate apoptosis (FACSCalibur, Becton, Dickinson & Co., USA).

Infrared thermal imaging in vivo

To further determine the photothermal effect of LPPFA in mice, we conducted a series of in vivo thermal imaging experiments. Five to seven days after subcutaneous inoculation of tumor cells (2×10^6 U14 cells) in the left armpit of the mice, LPPFA solution (5 mg/mL) was injected into the tail vein when the tumor volume reached 1000 mm^3. After 6 h, 808 nm-NIR-laser irradiation (2 W/cm^2) was performed and the infrared thermal photos were taken by the thermal imager (Tix580, FLUKE, USA) at scheduled time points. To further clarify the tumor-targeting property of LPPFA NPs, the nontumor sites in the contralateral axilla of tumors or tumor sites were also irradiated with an 808 nm laser for 10 min. The temperature changes at nontumor and tumor sites were detected and photographed using an infrared thermal imager (Tix580, FLUKE, USA).

Antitumor effect of LPPFA in vivo

After U14 cells were passaged in the abdominal cavity of mice, the cell density was adjusted to 1×10^7 cells/mL, and 0.2 mL of the cell suspension was subcutaneously injected into the left armpit of each mouse. After the inoculation, the mice were randomly divided into seven groups and each group was treated with the following: (1) normal saline (negative control), (2) PDA@PCN (PP) nanocarrier, (3) LPPA; (4) LPPA + 808 nm, (5) LPPFA + 808 nm, (6) LPPF + 808 nm + 660 nm, and (7) LPPFA + 808 nm + 660 nm. The mice in the different groups were administered the respective treatment every other day for 7 days. The laser irradiation was performed 6 h after the administration of treatment via the tail vein on the same day. The maximum and minimum diameters of the tumors were measured and recorded. The tumor volume was calculated using Eq. (6). The body weights of the mice in each group were recorded. On the 15th day of the experiment, the mice were euthanized using ether anesthesia and dissected under aseptic conditions. The tumor tissues and

major organs were harvested and weighed on an electronic balance. The organ indices were calculated using Eq. (7).

$$V_t = (L_{max} \times L_{min}^2)/2, \quad (6)$$

where V_t represents the tumor volume in mice, L_{max} is the maximum diameter of the tumors, and L_{min} stands for the minimum diameter of the tumors.

$$OI = m_o/m_{b,} \quad (7)$$

where OI stands for the organ index, m_o is the organ mass, and m_b is the body mass of the mouse on the day of sacrifice.

Pathological sections of the major organs (heart, liver, spleen, lungs, and kidneys) and the tumors from the LPPFA + 808 nm + 660 nm group were prepared using neutral buffered formalin. The tumor specimens from the normal saline and LPPFA + 808 nm + 660 nm treated groups were stained using hematoxylin–eosin (H&E), Ki67 immunohistochemistry and terminal deoxynucleotidyl transferase dUTP nick end labeling (TUNEL) to analyze the effects of LPPFA + 808 nm + 660 nm administration on the malignancy, cell proliferation, and apoptosis. Blood samples were collected from the mice in each group, including normal control, and used to assess the liver and kidney function markers (ALT, AST, BUN, CRE) according to the instructions on the reagent kits to evaluate the in vivo toxicity of LPPFA. During the entire experiment, the feeding, mental status, fecal color, and presence of excessive hair on the mice were monitored.

To further evaluate the photodynamic and chemodynamic therapeutic effects of LPPFA on the tumor tissues in vivo, the MDA levels and GSH activities were assessed using tumor tissue homogenates.

Statistical analysis

The images were merged using ImageJ software. Origin 2021 and GraphPad Prism 9 software were used for statistical analysis. Students' *t*-test (two groups) or one-way analysis of variance (ANOVA) was used to analyze data from two or more groups. All data were expressed as mean ± standard deviation. Differences with $P < 0.05$ were considered statistically significant.

Results and discussion

To construct the LPPFA NPs, PCN (Mn) was first synthesized using the solvothermal method. After loading LPC onto the metal–organic framework to obtain LPC@PCN, PDA was self-polymerized and coated onto the surface of LPC@PCN under alkaline conditions to obtain LPP. Next, Fe^{3+} and NH_2-AS1411 were sequentially modified on PDA through chelation and amide reactions, respectively, to form LPPFA (Scheme 1a). As shown in Fig. 1a, the TEM images revealed that the PCN (Mn) particles were square-shaped with a uniform average diameter of approximately 100 nm and good dispersity. Next, after loading LPC onto the PCN, LPP was generated by coating PDA on the PCN (Mn) surface via DA oxidative polymerization. LPP possessed a core-shell spherical structure with a particle size of about 160 nm (Fig. 1b). Particle size analysis showed that the hydrodynamic diameter of the PCN NPs was (80 ± 3.4) nm. After loading of LPC and wrapping PDA, it increased to (142 ± 7.3) nm, which further proved that PDA formed a coating structure with a certain thickness on the surface of PCN (Fig. 1c). UV–Vis spectrum analysis was performed to confirm the successful loading of LPC on PCN, which showed a distinct absorbance peak corresponding to LPC at 430 nm (Fig. 1d). This confirmed the LPC encapsulation on PCN with high loading efficiency. The zeta potentials of various NPs were measured to demonstrate the successful synthesis of LPPFA. As shown in Fig. 1e, the PCN NPs were negatively charged with a zeta potential of (− 8.2 ± 0.8) mV, while it was (− 15.5 ± 1.2) mV for LPP due to the PDA coating. The zeta potential of LPPF nanoparticles increased to (−5.2 ± 0.3) mV again due to the presence of Fe^{3+} on the PDA surface. The zeta potential of the LPPFA nanoparticles decreased to (−6.4 ± 0.5) mV after the negatively charged AS1411 was linked. The SEM energy spectrum analysis further confirmed the successful chelation of Fe^{3+} on LPPFA (Fig. 1f). The successful modification of AS1411 on LPPFA was verified using agarose gel electrophoresis. As shown in Fig. 1g, free AS1411, a single-stranded DNA aptamer with only 26 bases, migrated over a long distance due to its small size (Lane 2). LPPFA, created by linking AS1411 and LPPF via amide reaction, has a higher molecular weight and hence, it hardly migrated and remained near the sample pore, as compared to the band corresponding to the free AS1411, which might exist due to incomplete linkage in the LPPFA sample (Lane 3).

After successfully preparing LPPFA, we further evaluated its stability and acid responsiveness. DLS was performed on the NPs for five days, which showed no significant changes in the particle size of the NPs from Day 1 to Day 5, and all NPs remained around 160 nm in diameter (Fig. 1h). This indicated that the LPPFA NPs were highly stable and dispersible in serum. Figure 1i showed that LPPFA degraded into irregular fragments under acidic conditions due to the acid sensitivity of PDA.

We evaluated the photothermal performance of the PDA in LPPFA using PCN and LPPFA with water as a blank control. As shown in Fig. 2a, after irradiation with an 808 nm NIR laser (2 W/cm^2), the temperature of both water and PCN solution did not change significantly, while that of the LPPFA solution (1 mg/mL) increased from room temperature of 25°C to 52 °C after 10 min of laser irradiation. This

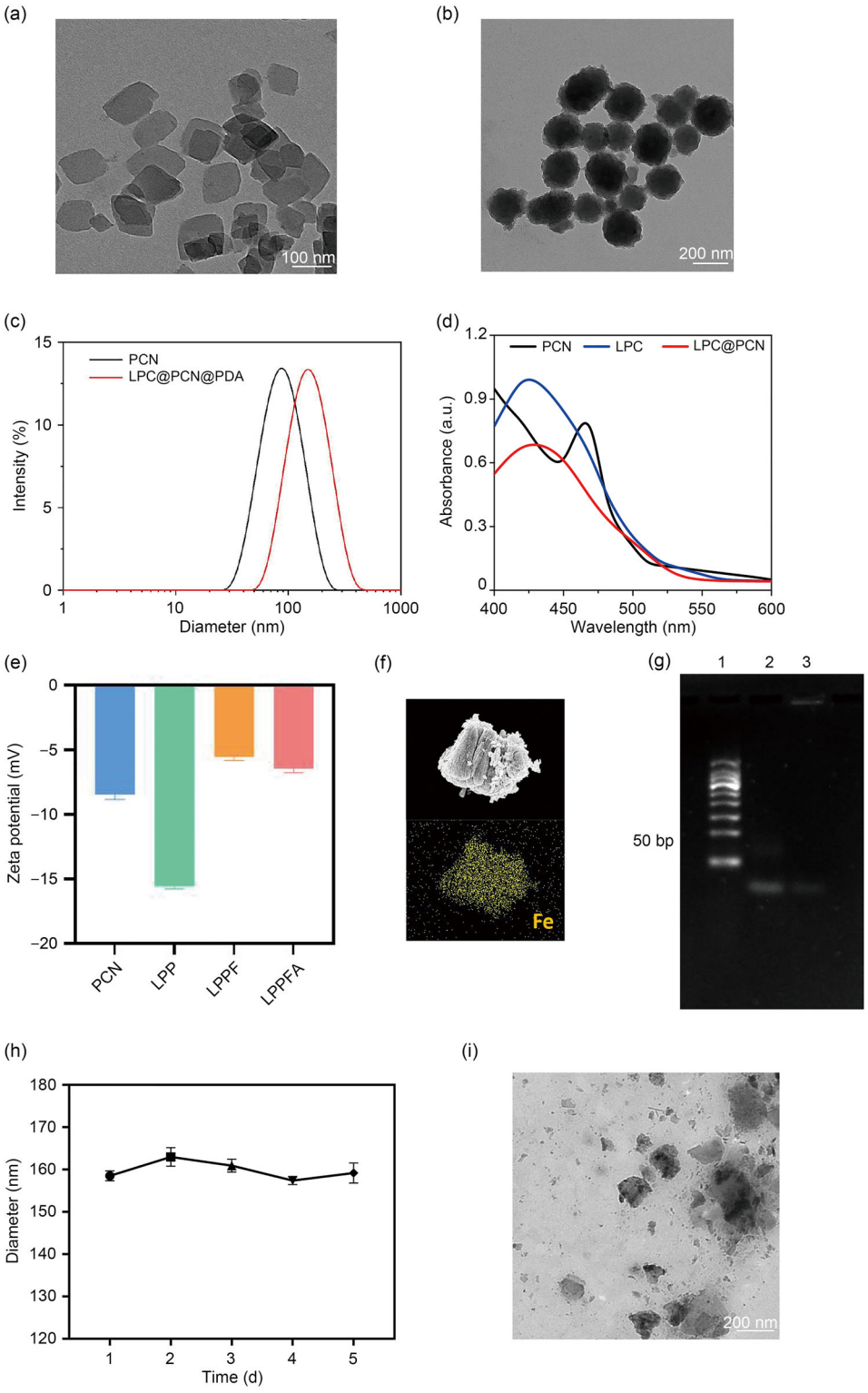

Fig. 1 Characterization of LPPFA nanoparticles. Representative TEM images of **a** PCN and **b** LPC@PCN@PDA. **c** Hydrodynamic size distribution of PCN and LPC@PCN@PDA. **d** UV-absorbance spectrum of PCN, LPC, and LPC@PCN. **e** Zeta potential changes during the synthesis process of LPPFA. **f** Representative SEM image of LPPFA and corresponding Fe element mapping of LPPFA. **g** Agarose gel electrophoresis image of AS1411 and the reaction product of LPPFA. **h** Stability test of LPPFA nanoparticles in serum. **i** Representative TEM image of LPPFA nanoparticles in an acidic environment (pH: 5.5). Data are represented as mean ± standard deviation ($n = 3$) in (e, h). LPPFA: LPC@PCN@PDA/Fe^{3+}-AS1411; LPC: β-lapachone; PCN: porous coordination network; PDA: polydopamine; TEM: transmission electron microscopy; UV: ultraviolet; SEM: scanning electron microscope; LPP: LPC@PCN@PDA; LPPF: LPC@PCN@PDA/Fe^{3+}

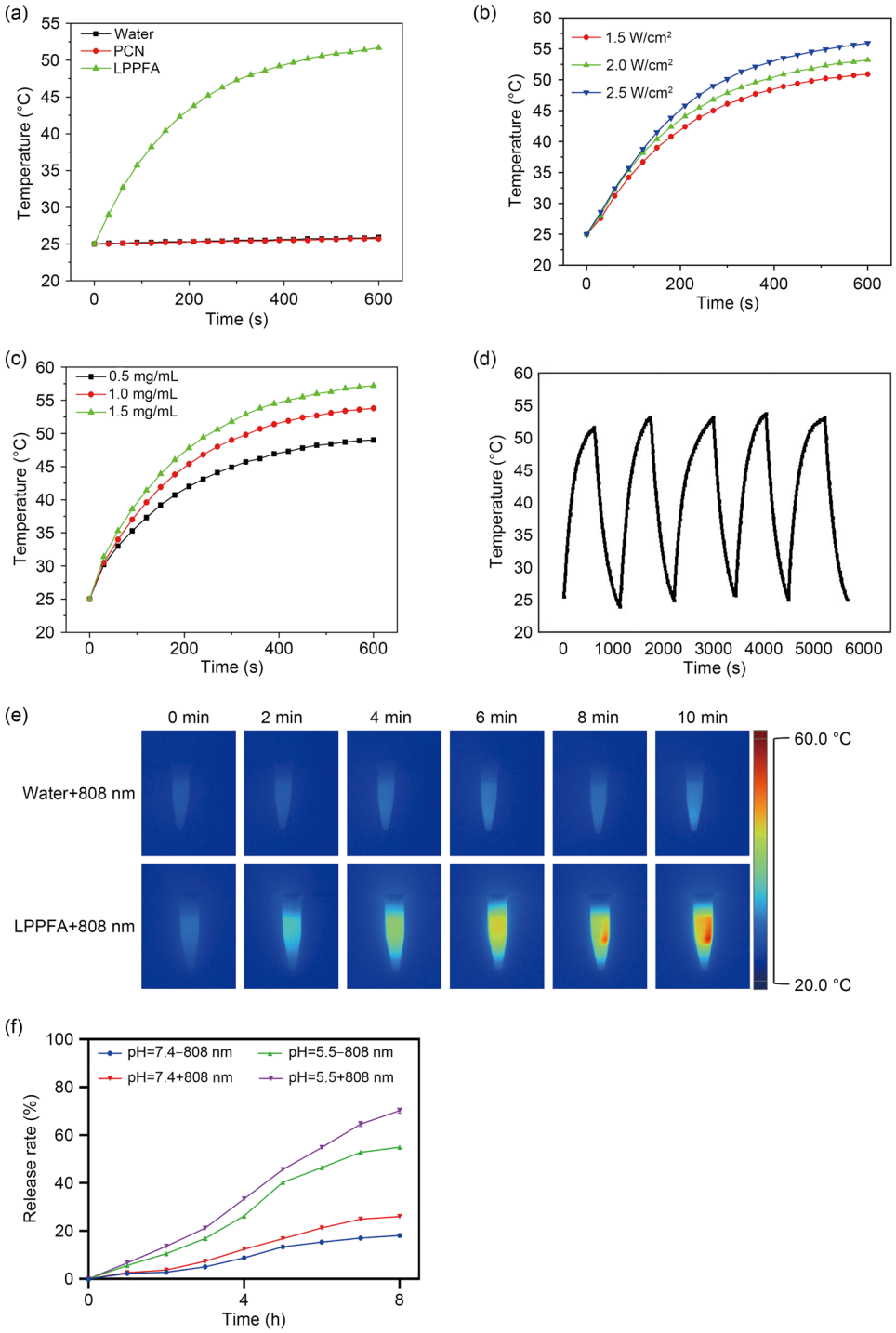

Fig. 2 Photothermal properties and drug release profile of LPPFA nanoparticles. The temperature rise curves of **a** water, PCN, and LPPFA under 808 nm NIR laser irradiation (2 W/cm^2), **b** LPPFA under different laser powers, and **c** LPPFA under different concentrations. **d** Temperature rise and fall curve of LPPFA. **e** Infrared thermal images of LPPFA solution at different time interval irradiations. **f** Drug release profiles of LPPFA in different environments. LPPFA: LPC@PCN@PDA/Fe^{3+}-AS1411; LPC: β-lapachone; PCN: porous coordination network; PDA: polydopamine; NIR: near-infrared

indicated that LPPFA possessed good photothermal conversion performance due to the PDA coating, which was directly related to the laser power and solution concentration (Figs. 2b and 2c). To verify its photothermal stability, we conducted five photothermal switching cycles using LPPFA (1 mg/mL, NIR laser power 2 W/cm^2). We observed that the temperature of the LPPFA NPs was still able to rise to that after the first irradiation within a certain period, even after repeated irradiation, indicating that LPPFA possessed an ideal photothermal stability (Fig. 2d). Furthermore, the temperature change of LPPFA was better visualized by real-time thermal imaging photos (Fig. 2e). Upon quantifying the photothermal conversion performance of LPPFA, the photothermal conversion efficiency was found to be 47.9% according to the heating-and-cooling curve. The regional hyperthermia generated by

photothermal conversion is effective for photothermal therapy (PTT) of malignant tumors [20].

To determine the EE and DL of LPC in LPPFA NPs, a standard curve was plotted using the absorbances at 430 nm and different LPC concentrations. The EE and DL of LPC in LPPFA were determined to be (92.15 ± 1.00)% and (5.55 ± 0.47)%, respectively, indicating that LPC was efficiently loaded into the porphyrin PCN (Mn) framework.

After that, the pH- and 808 nm irradiation-triggered release behaviors of LPPFA were investigated in PBS (at pH of 7.4 or 5.5) with or without 808 nm laser irradiation (2 W/cm^2, 10 min). LPC was released much more rapidly in an acid environment (pH = 5.5) than under neutral conditions (pH = 7.4) (Fig. 2f). After 8 h, the release rate of LPC could reach (57.4 ± 0.7)% in an acidic environment, while it was only (17.6 ± 0.5)% in a neutral environment, indicating the pH-responsive release of LPC from LPPFA. Both in neutral and acidic conditions, 808 nm laser irradiation further promoted the release of LPC from the LPPFA solution. Under acidic conditions along with laser irradiation, the LPC release rate was increased to (78.2 ± 1.0)% after 8 h, while under neutral conditions with laser irradiation, the LPC release rate reached (21.3 ± 0.8)%. These results showed the dual responsive LPC release from LPPFA under specific pH and 808 nm irradiation conditions. This effect was due to acid degradation and the heat generated by the photothermal effect of PDA, which promotes the molecular movement to enhance the chemotherapeutic effect of LPC further.

The ability of LPPFA to catalyze H_2O_2 to produce ·OH was evaluated using MB as an indicator. ·OH radicals can oxidize MB from blue to colorless at a maximum absorbance of 654 nm. H_2O_2 (1 mmol/L) was supplemented in the MB solutions to simulate the H_2O_2 levels inside tumor cells. The fading of the blue color in LPPFA solution containing H_2O_2 and MB was more significant with increased LPPFA concentration (Fig. 3a). When the concentration reached 1 mg/mL, the solution turned almost colorless, suggesting the occurrence of the Fenton reaction in the presence of H_2O_2 due to the chelated iron ions. This effect can be used for CDT against malignant tumors.

As ROS are essential for the therapeutic effect of PDT, the ROS production capacity of LPPFA NPs was further monitored by the DPBF elimination method [21]. As shown in Fig. 3b, the absorbance at 417 nm of LPPA solution with H_2O_2 and DPBF decreased significantly under 660 nm laser irradiation due to the fluorescence quenching of DPBF by the generated ROS. Compared with the LPPA solution, the quenching caused by LPPFA was more significant, indicating that the chelated Fe^{3+} on LPPFA promoted O_2 production via the Fenton effect, thereby generating more ROS, which enhanced the PDT effect.

To further determine the intracellular photodynamic performance of LPPFA, DCFH-DA was used as a ROS probe. No green fluorescence was observed in the PBS-treated cells, indicating an extremely low cellular ROS content (Fig. 3c). Moderate green fluorescence was generated in the LPC-treated cells as the catalysis of LPC by NQO1 in tumor cells selectively increases the ROS levels in cancer cells. The cells treated with PPA and 660 nm laser irradiation produced strong green fluorescence, indicating that the photodynamic properties of the porphyrin organometallic framework oxidized the cellular macromolecules to produce ROS. The fluorescence intensity of cells treated with LPPA followed by 660 nm was stronger than that of the PPA + 660 nm laser irradiation group due to LPC's photodynamic properties and the ROS produced by NQO1-mediated catalysis. Meanwhile, the fluorescence intensity of the cells treated with LPPFA combined with laser irradiation was the strongest. This indicated the highest ROS production due to the combined action of the photodynamic properties of porphyrin on PCN (Mn) and Fe^{3+}-mediated hydrolysis of H_2O_2 of LPPFA via the Fenton reaction, which further enhanced the photodynamic properties of porphyrin of PCN (Mn). Moreover, more H_2O_2 was produced by the LPC, which was the substrate of the Fenton reaction during catalysis by NQO1, further enhancing the photodynamic performance of PCN (Mn).

To explore the effective accumulation of LPPFA NPs inside the cells mediated by the targeting effect of AS1411, the uptake of NPs by HeLa cells was detected using fluorescence microscopy and FCS with fluorescein FITC labeled-LPPA and LPPFA, respectively. As shown in Fig. 4a, the uptake of NPs was higher in the LPPFA-treated cells than that in the LPPF-treated cells, indicating that AS1411 promoted the uptake of NPs into cells by binding to the nucleolin overexpressed on the tumor cell membrane. This enhanced the tumor active targeting of LPPFA NPs, further confirmed by the FCS results (Fig. 4b).

To further evaluate the inhibitory effect of LPPFA NPs on cell proliferation in vitro, HMVECs and HeLa cells were cultured for CCK-8 assay. As shown in Fig. 4c, treatment with different concentrations of PCN@PDA did not significantly inhibit cell proliferation compared with PBS-treated cells, indicating that the nanocarrier had good biosafety. The LPPFA NPs had a weak cytotoxic on the proliferating cells, even at a 100 μg/mL concentration, as the cell survival rate was still (77.3 ± 1.2)%. The presence of less nucleolin on the surface of normal epithelial cells decreases the uptake of NPs by these cells. Moreover, only LPC was released to achieve chemotherapy by inhibiting DNA polymerase without laser irradiation. Next, we further evaluated the inhibitory effect of different NPs combined with laser irradiation on tumor cells (Fig. 4d). HeLa cells treated with varying concentrations of PP nanoparticles maintained high viability without any significant inhibition of cell proliferation, indicating that the empty carrier possessed good biosafety. The LPC, LPPA + 808 nm, LPPFA + 808 nm, and LPPFA +

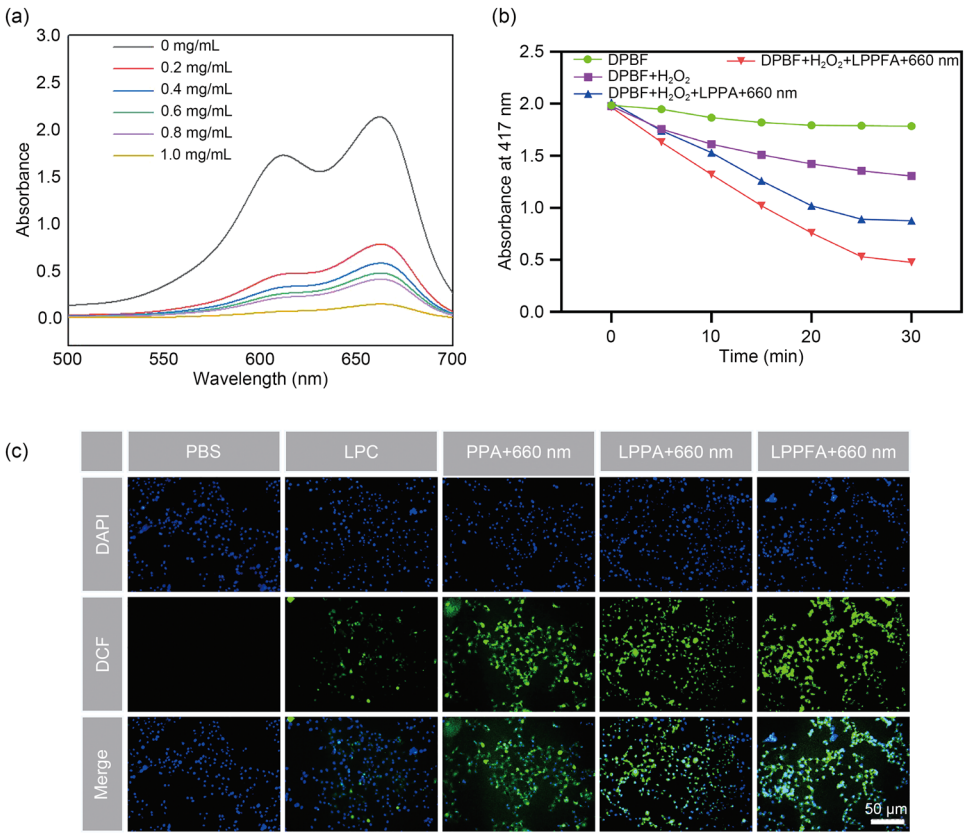

Fig. 3 Hydroxyl radical and ROS are produced by LPPFA nanoparticles in vitro and in vivo. Effect of LPPFA + 660 nm on the in vitro production of **a** ·OH and **b** ROS. **c** Effect of different nanodrugs on intracellular ROS production. ROS: reactive oxygen species; LPPFA: LPC@PCN@PDA/Fe^{3+}-AS1411; LPC: β-lapachone; PCN: porous coordination network; PDA: polydopamine; DPBF: diphenylbenzofuran; PBS: phosphate buffer saline; PPA: PCN@PDA/AS1411; LPPA: LPC@PCN@PDA/AS1411; DAPI: 4,6-diamino-2-phenylindole; DCF: 2′,7′-dichlorofluorescein

808 nm + 660 nm treatment groups showed similar inhibition effects on cell proliferation at a concentration of 12.5 μg/mL, with cell survival rates of (75 ± 2.5)%. The tumor cell survival rate decreased significantly with an increase in the concentration of NPs in each group. The cell viability of the LPPFA + 808 nm + 660 nm treatment group was the lowest and the tumor cell survival rate was only (12.7 ± 3.1)% at a concentration of 100 μg/mL. Tumor proliferation was also inhibited in the other groups (LPC, LPPA + 808 nm, and LPPFA + 808 nm), indicating that chemotherapy using a single drug, PTT and aptamer, and PTT-enhanced CDT and aptamer, all exerted potent tumor growth inhibition effect. The multimodal combination of synergistic enhanced chemotherapy–PTT–enhanced PDT–enhanced CDT exhibited the most effective antitumor effect.

To further verify the multimodal effect of LPPFA NPs on HeLa cells, live/dead cell fluorescence staining was conducted. As shown in Fig. 4e, compared with the PBS-treated group, treatment with free LPC exerted a chemotherapeutic effect by inhibiting tumor growth. This effect was stronger in the LPPA + 808 nm treatment group due to the enhanced chemotherapy mediated by the PTT and aptamer combination. Compared with LPPA + 808 nm treatment, LPPFA + 808 nm treatment manifested more significant cytotoxicity on HeLa cells due to the combined effect of PTT-enhanced aptamer-mediated CDT. Moreover, the LPPFA + 808 nm + 660 nm treatment group demonstrated a potent inhibitory effect and the strongest cytotoxic effects on HeLa cells due to the synergistic action of PDT and CDT enhanced by PTT and aptamer.

Rhodamine 123 can enter the mitochondria of living cells and emit bright yellow–green fluorescence. The intensity of this fluorescence is significantly reduced during cellular apoptosis or necrosis. Compared with the PBS-treated cells, this fluorescence was significantly decreased in free LPC-treated cells, indicating that LPC acted on topoisomerase in the nucleus to induce apoptosis in tumor cells, thus decreasing the mitochondrial membrane potential. This fluorescence intensity was significantly reduced in the LPPFA + 808 nm treated group, indicating further loss of mitochondrial membrane potential in HeLa cells due to the enhanced chemotherapeutic effect by the combined action of PTT-enhanced aptamer-mediated CDT. The mitochondrial membrane potential in the cells treated with LPPFA + 808 nm + 660 nm was further reduced compared with the LPPFA + 808 nm treatment cells, indicating the presence of more apoptotic cells in the latter group (Fig. 4f). The results of cellular apoptosis quantified using FCS with an Annexin V-FITC/PI apoptosis detection kit were consistent with the previous findings. Figure 4g showed that LPPFA + 808 nm + 660 nm treatment could induce cellular apoptosis up to (30.71 ± 1.6)%, which was much higher than that of LPC

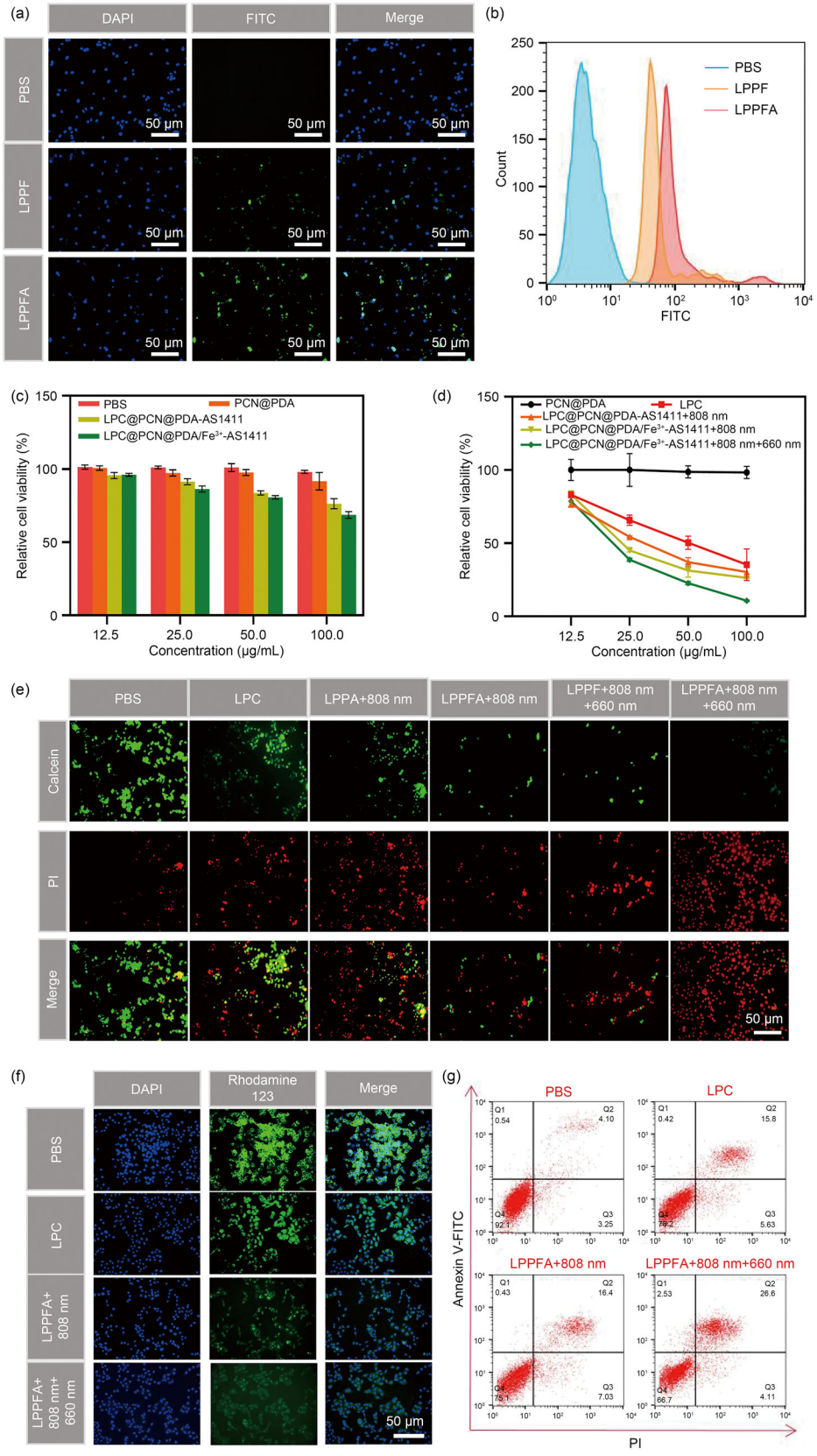

Fig. 4 Cellular uptake and cytotoxicity profile of LPPFA nanoparticles. **a** Fluorescence images of LPPFA in HeLa cells. **b** Flow cytometry quantification of fluorescence intensity in HeLa cells treated with PBS, LPPF, and LPPFA. Effect of nanoparticles on the **c** cell viability of HMVECs and **d** HeLa cells (combined with NIR laser irradiation). **e** Fluorescent images of live/dead staining of tumor cells. **f** Changes in intracellular mitochondrial membrane potential after treatment with different nanoparticles. **g** Flow cytometry analysis of the apoptosis-inducing effect of different nanoparticles. Data are represented as mean ± standard deviation ($n = 3$) in (c, d). LPPFA: LPC@PCN@PDA/Fe^{3+}-AS1411; LPC: β-lapachone; PCN: porous coordination network; PDA: polydopamine; PBS: phosphate buffer saline; LPPF: LPC@PCN@PDA/Fe^{3+}; HMVECs: human lung microvascular endothelial cells; NIR: near-infrared; DAPI: 4,6-diamino-2-phenylindole; FITC: fluorescein isothiocyanate

((21.43 ± 1.6)%) and LPPFA + 808 nm ((23.43 ± 1.5)%) treatment groups.

To further explore the feasibility of LPPFA for PTT and achieve better drug accumulation in tumor tissues, we established mice cervical cancer models combined with in vivo thermal imaging to study the in vivo photothermal performance and tumor targeting effect of LPPFA NPs (Fig. 5a). After the mice were intravenously injected with saline, the temperature of the tumor site did not change significantly after 10 min of NIR laser irradiation, indicating that the physical irradiation of laser did not increase the temperature of tumors (Fig. 5b). However, the temperature of the tumor sites gradually increased under NIR 808 nm laser irradiation for 6 h after the LPPFA NP injection, reaching 53 °C after 10 min of irradiation. This showed the successful accumulation and good photothermal conversion efficiency of LPPFA NPs in the tumor sites of mice. Six hours after intravenous injection of LPPFA NPs, no noticeable temperature changes were seen in the contralateral nontumor sites irradiated by the 808 nm laser for 10 min (Fig. 5c). These findings indicated that the circulating NPs successfully targeted and accumulated in the tumor sites due to passive targeting by the enhanced permeability and retention (EPR) effect and specific targeting by AS1411 to exert a photothermal conversion effect.

To assess the antitumor effect of LPPFA + 808 nm + 660 nm laser irradiation in vivo, we established cervical cancer mice models by subcutaneously inoculating U14 cells into the mice axilla. The established models were randomly divided into seven groups ($n = 5$ mice/group) and administered with the following: (1) normal saline (negative control), (2) PP nanocarrier, (3) LPPA, (4) LPPA + 808 nm laser, (5) LPPFA + 808 nm laser, (6) LPPF + 808 nm + 660 nm laser, and (7) LPPFA + 808 nm + 660 nm laser. Different nanomaterials were injected into the tail vein and 6 h later, the mice were irradiated with 808 nm or/and 660 nm laser (Fig. 5d). As shown in Figs. 5e and 5f, compared with the normal saline group, tumor growth inhibition in the PP treatment group was insignificant, further confirming PP's biosafety as a nanodrug carrier material. However, LPPA significantly inhibited tumor growth due to the combined effect of LPC and AS1411. After treatment with LPPA + 808 nm laser irradiation, the tumor growth was further decreased due to the enhanced chemotherapeutic effect mediated by PTT and AS1411. The tumor growth was significantly reduced in the mice treated with LPPFA + 808 nm as the Fe^{3+} ions improved the CDT effect along with PTT and AS1411. Compared with the LPPFA + 808 nm treatment group, the tumor growth rates of mice in the LPPF + 808 nm + 660 nm and LPPFA + 808 nm + 660 nm treatment groups were further decreased because of enhanced PDT. However, there was no significant difference between these two groups. We speculated that this might be due to the limited number of AS1411 linked to the delivery system and the lack of any therapeutic effect of AS1411 in vivo. After 13 days of treatment with different NPs, the tumor weight of mice was measured (Fig. 5g). The tumor inhibition rates of the LPPA, LPPA + 808 nm, and LPPFA + 808 nm treatment groups were (51.2 ± 2.1)%, (73.3 ± 3.1)%, and (78.7 ± 4.3)%, respectively. LPPF + 808 nm + 660 nm and LPPFA + 808 nm + 660 nm treatment groups achieved similar tumor inhibition effects with tumor inhibition rates of (87.6 ± 2.8)% and (88.3 ± 3.0)%, respectively, consistent with the results of the tumor volume growth curve.

To further understand the mechanism of inhibition of tumor proliferation by LPPFA NPs combined with sequential irradiation with 808 nm and 660 nm lasers, we performed H&E, Ki67 immunohistochemical (IHC), and TUNEL staining assays on the tumor tissue slices from saline-treated control and LPPFA + 808 nm + 660 nm treated mice, respectively (Fig. 6a). The H&E staining results showed that compared with the normal saline treatment group, the tumor tissues of the LPPFA-treated mice showed more pink areas and reduced nucleocytoplasmic ratios in the cells, indicating that the tumor cells had undergone apoptosis or necrosis. This showed that malignancy of the tumor tissue was significantly reduced. Ki67 IHC staining results indicated that LPPFA-treated mice displayed a substantially lower positivity rate for Ki67 than the saline control group, indicating significant inhibition of tumor growth. The results of the one-step TUNEL apoptosis assay showed that compared with the normal saline treatment group, obvious green fluorescence was observed in the tumor tissue sections of the LPPFA + 808 nm + 660 nm treatment group, indicating that this treatment exerted a potent therapeutic effect on tumor tissues, inducing their apoptosis.

As a photosensitizer, PCN can produce ROS and cause lipid peroxidation under aerobic and light conditions [22]. Furthermore, LPC-loaded in LPPFA can generate ROS under the action of quinone oxidoreductase. Meanwhile, the Fe^{3+} induced by LPPFA byproducts can act as a CDT substrate to accelerate CDT and produce more ·OH, further increasing the oxidative damage and causing lipid peroxidation of tumor tissues. Meanwhile, as GSH was consumed during the conversion of Fe^{3+} to Fe^{2+} during CDT, we used MDA levels and GSH content as indicators to analyze the changes in redox balance in the tumor tissues after LPPFA treatment. Compared with the normal saline treatment group, the MDA content in the LPPFA + 808 nm treatment group was moderately elevated, indicating that LPC generated ROS under the action of quinone oxidoreductase and Fe^{3+} induced CDT, resulting in lipid peroxidation of tumor cells. The MDA levels in the LPPFA + 808 nm + 660 nm and LPPFA + 808 nm + 660 nm treatment groups were increased significantly compared with the LPPFA + 808 nm treatment group, indicating further enhancement of PDT induced by PCN. The MDA content in the LPPFA + 808 nm + 660 nm treatment group

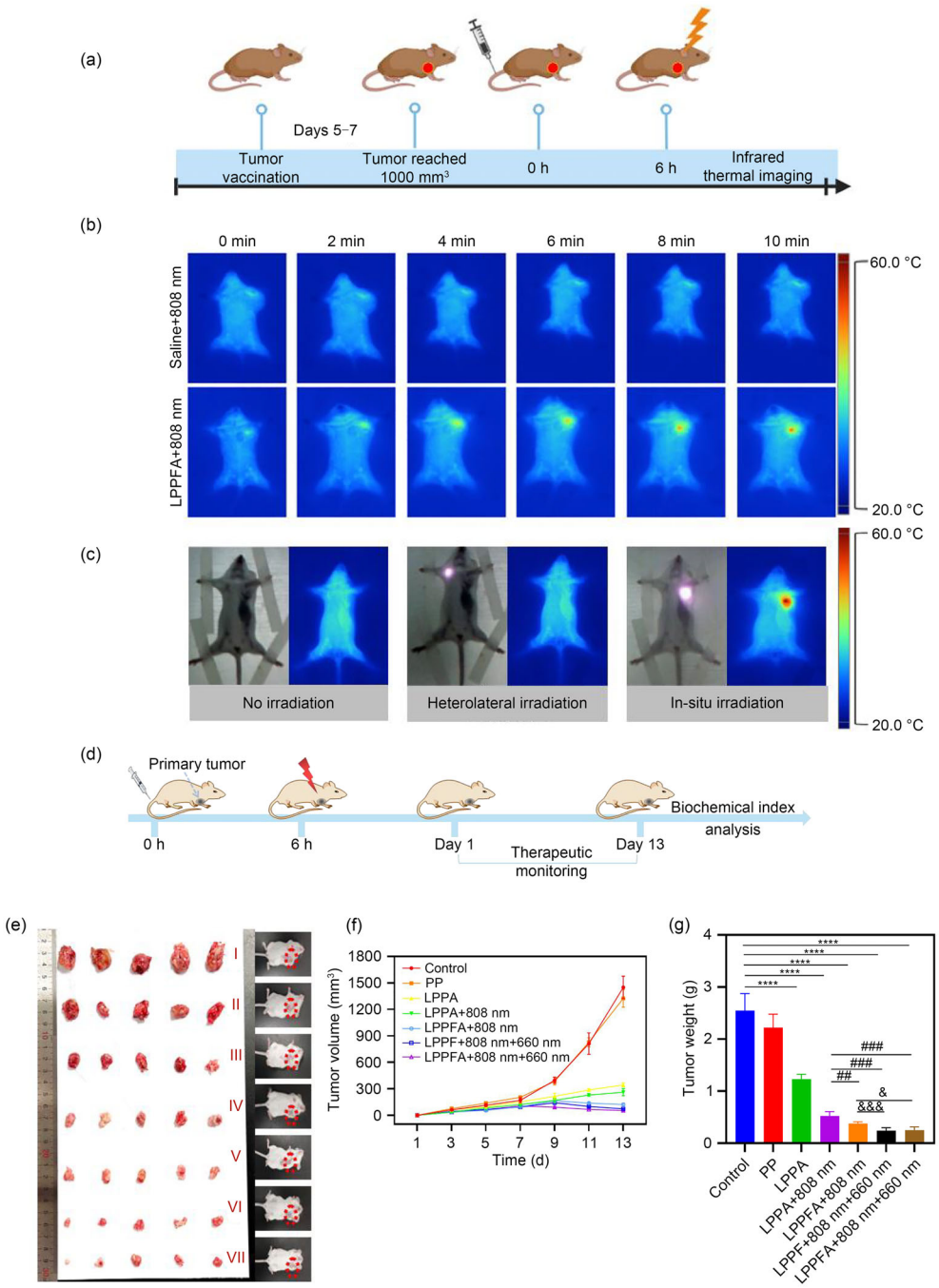

Fig. 5 In vivo tumor targeting and synergistic antitumor effects of LPPFA nanoparticles. **a** Schematic diagram of in vivo thermal imaging. Infrared thermal images of **b** mice injected with saline and LPPFA under 808 nm laser irradiation (2 W/cm^2) for 10 min and **c** different locations of tumor-bearing mice irradiated with 808 nm laser (2 W/cm^2) 6 h after injection. **d** Schematic diagram of the treatment procedure for the U14 tumor-bearing mice models. **e** Images of tumor tissues with different treatment regimens on Day 13 of the experiment. **f** Tumor growth curves and **g** tumor weights of mice from different treatment groups on Day 13. Data are represented as mean ± standard deviation ($n = 5$) in (f, g). $^{****}P < 0.0001$ compared with the normal saline control group; $^{###}P < 0.001$ and $^{##}P < 0.01$ compared with the LPPA + 808 nm treatment group; $^{\&}P<0.05$ and $^{\&\&\&}P<0.001$ compared with the LPPFA + 808 nm treatment group. LPPFA: LPC@PCN@PDA/Fe^{3+}-AS1411; LPC: β-lapachone; PCN: porous coordination network; PDA: polydopamine; PP: PDA@PCN; LPPA: LPC@PCN@PDA/AS1411; LPPF: LPC@PCN@PDA/Fe^{3+}

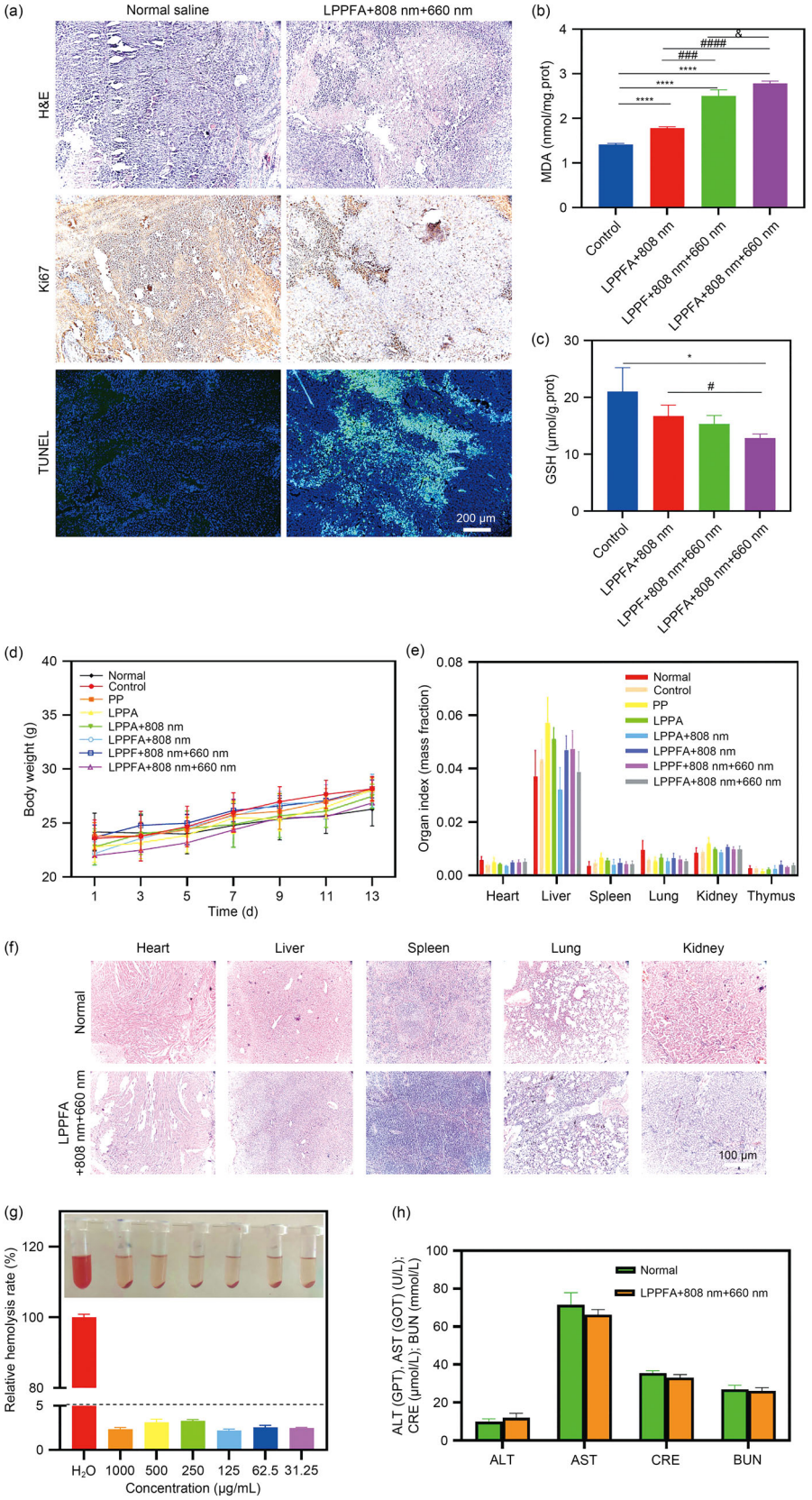

Fig. 6 Tumor inhibition mechanism of LPPFA and safety evaluation in vivo. Images of tumor tissues from LPPFA-treated mice subjected to **a** H&E, Ki67 immunohistochemical, and TUNEL staining (magnification: 10 × 20). Changes in **b** the MDA activity, **c** GSH content in tumor tissues, and **d** the body weight of tumor-bearing mice treated with different drugs. **e** Effect of different drug treatments on the organ indices of tumor-bearing mice. **f** Observation of pathological sections of major organs in LPPFA + 808 nm + 660 nm treated group (magnification: 10 × 20). **g** Hemolysis rate at different LPPFA concentrations. **h** Effect of LPPFA on liver and kidney function indicators. Data are represented as mean ± standard deviation ($n = 5$) in (b–e) and (g, h). $^{****}P < 0.0001$ and $^{*}P < 0.05$ compared with the normal saline control group; $^{\#\#\#\#}P < 0.0001$, $^{\#\#\#}P < 0.001$, and $^{\#}P < 0.05$ compared with the LPPFA + 808 nm treatment group; $^{\&}P < 0.05$ compared with the LPPF + 808 nm + 660 nm treatment group. LPPFA: LPC@PCN@PDA/Fe^{3+}-AS1411; LPC: β-lapachone; PCN: porous coordination network; PDA: polydopamine; H&E: hematoxylin–eosin; TUNEL: terminal deoxynucleotidyl transferase dUTP nick end labeling; MDA: malondialdehyde; GSH: glutathione; LPPF: LPC@PCN@PDA/Fe^{3+}; PP: PDA@PCN; LPPA: LPC@PCN@PDA/AS1411; ALT: alanine transaminase; AST: aspartate aminotransferase; CRE: creatinine; BUN: blood urea nitrogen; GPT: glutamic pyruvic transaminase; GOT: glutamic oxalacetic transaminase

was higher than that in the LPPF + 808 nm + 660 nm treatment group, possibly due to active targeting by AS1411, in increasing the accumulation of NPs in tumor tissues (Fig. 6b). The GSH content in the tumor tissues in the different groups was lower than that in the saline control group, with the lowest level seen in the LPPFA + 808 nm + 660 nm treatment group. This indicated the increased consumption of GSH in tumor tissues, which enhanced the PDT, CDT, and chemotherapeutic effects (Fig. 6c). These experiments further verified that treatment with LPPFA + 808 nm + 660 nm achieved enhanced chemotherapy due to the synergistic action of PDT and CDT.

As shown in Figs. 6d and 6e, there were no significant changes in mice's body weight and organ index in the different treatment groups, indicating the lack of toxic side effects on mice. To further evaluate the biosafety of LPPFA NPs in vivo, pathological observations were performed using the significant organs (heart, liver, spleen, lungs, and kidneys) of the mice in the LPPFA + 808 nm + 660 nm treatment group 13 days after drug administration (Fig. 6f). The results showed that the tissue structure of each organ in the LPPFA + 808 nm + 660 nm treated group was similar to that of the normal control group without any tissue damage, degeneration, or edema. This validated that the LPPFA NPs showed negligible in vivo cytotoxicity.

We further conducted a hemolysis assay to verify the safety of LPPFA nanoparticles in blood circulation. As shown in Fig. 6g, the hemolysis rates in the groups treated with different concentrations of LPPFA NPs were all lower than 5%, indicating that LPPFA NPs could be safely transported in blood with low hemolytic toxicity for intravenous administration.

To further clarify whether the treatment of LPPFA NPs exerted hepato- or renal-toxicity on tumor-bearing mice, the biochemical indices of liver and kidney functions (CRE, BUN, AST/GOT, ALT/GPT) of LPPFA-treated mice and normal mice were tested (Fig. 6h). There were no significant changes in the levels of all these indicators in the serum of LPPFA-treated mice compared with the normal mice group, indicating that LPPFA + 808 nm + 660 nm treatment displayed no significant toxic effects on the liver and kidneys of the tumor-bearing mice. However, the acute and sub-acute toxicity of these nanoparticles need to be systematically analyzed in the future.

Conclusions

In summary, we successfully developed a light/pH-dual-smart responsive nanodrug delivery platform to overcome tumor hypoxia and achieve the enhanced effect of combined PDT, CDT, and chemotherapy. LPC and PCN were specifically released into the tumor microenvironment via acid-responsive degradation of PDA and fully accumulated at the tumor site. LPC binds to topoisomerase to cause the accumulation of positive DNA superhelix, thus effectively inhibiting tumor cell proliferation. The Fe^{3+} chelated on the surface of the PDA coating catalyzed the generation of O_2 from the excess H_2O_2 in the tumor environment, which effectively increased the ROS level generated by LPC and the porphyrin photosensitizer, boosting the tumor inhibitory. Meanwhile, the Fe^{2+} generated during catalysis via the Fenton reaction that produced ·OH, caused lipid peroxidation in tumor cells to exert CDT. Experiments in vitro and in vivo revealed that the NPs demonstrated specific tumor targeting, excellent tumor growth inhibition effect, and biocompatibility. Taken together, our findings can facilitate the development of an intelligent multifunctional therapeutic nanoplatform for cancer therapy.

Acknowledgements This work was supported by the National Natural Science Foundation of China (No. 62071413), the Hebei Natural Science Foundation of China (Nos. C2019203556 and F2020203056), and the Natural Science Foundation of Hebei Province for Innovation Group Project, China (No. C2022203003).

Author contributions SHL collected the literature and wrote the manuscript. SHL, XZ, ZMB, YBY, and JZ prepared the scientific illustrations and experimental data. SHL, YBY, and JL proofread and finalized the revised manuscript. KL, ZWL, MS, LXD, JDW, and JL conceived the manuscript, prepared, and approved the final version of the manuscript.

Declarations

Conflict of interest The authors declare that they have no conflict of interest.

Ethical approval All experimental operations were approved by the Animal Care and Use Committee of Yanshan University in China (Ethical number: YD2022011).

References

1. Bu LL, Yan JJ, Wang ZJ et al (2019) Advances in drug delivery for post-surgical cancer treatment. Biomaterials 219:119182. https://doi.org/10.1016/j.biomaterials.2019.04.027
2. Arranja AG, Pathak V, Lammers T et al (2017) Tumor-targeted nanomedicines for cancer theranostics. Pharmacol Res 115:87–95. https://doi.org/10.1016/j.phrs.2016.11.014
3. Alshehri S, Imam SS, Rizwanullah M et al (2020) Progress of cancer nanotechnology as diagnostics, therapeutics, and theranostics nanomedicine: preclinical promise and translational challenges. Pharmaceutics 13(1):24. https://doi.org/10.3390/pharmaceutics13010024
4. Liu JT, Liu TR, Du P et al (2019) Metal-organic framework (MOF) hybrid as a tandem catalyst for enhanced therapy against hypoxic tumor cells. Angew Chem Int Ed Engl 58(23):7808–7812. https://doi.org/10.1002/anie.201903475
5. Han K, Ma ZY, Han HY (2018) Functional peptide-based nanoparticles for photodynamic therapy. J Mater Chem B 6(1):25–38. https://doi.org/10.1039/c7tb02804k

6. Ruiz-González R, Milán P, Bresolí-Obach R et al (2017) Photodynamic synergistic effect of pheophorbide a and doxorubicin in combined treatment against tumoral cells. Cancers 9(2):18. https://doi.org/10.3390/cancers9020018
7. Sunassee SN, Veale CG, Shunmoogam-Gounden N et al (2013) Cytotoxicity of lapachol, beta-lapachone and related synthetic 1,4-naphthoquinones against oesophageal cancer cells. Eur J Med Chem 62:98–110. https://doi.org/10.1016/j.ejmech.2012.12.048
8. Li XS, Kwon N, Guo T et al (2018) Innovative strategies for hypoxic-tumor photodynamic therapy. Angew Chem Int Ed Engl 57(36):11522–11531. https://doi.org/10.1002/anie.201805138
9. Liu YD, Zhou ZW, Liu YD et al (2019) H_2O_2-activated oxidative stress amplifier capable of GSH scavenging for enhancing tumor photodynamic therapy. Biomater Sci 7(12):5359–5368. https://doi.org/10.1039/c9bm01354g
10. Tian HL, Zhang MZ, Jin GX et al (2021) Cu-MOF chemodynamic nanoplatform via modulating glutathione and H_2O_2 in tumor microenvironment for amplified cancer therapy. J Colloid Interface Sci 587:358–366. https://doi.org/10.1016/j.jcis.2020.12.028
11. Gaschler MM, Stockwell BR (2017) Lipid peroxidation in cell death. Biochem Biophys Res Commun 482(3):419–425. https://doi.org/10.1016/j.bbrc.2016.10.086
12. Gao M, Meng X, Guo XL et al (2018) All-active antitumor micelles via triggered lipid peroxidation. J Control Release 286:381–393. https://doi.org/10.1016/j.jconrel.2018.08.003
13. Zhuang HQ, Su HL, Bi XX et al (2017) Polydopamine nanocapsule: a theranostic agent for photoacoustic imaging and chemo-photothermal synergistic therapy. ACS Biomater Sci Eng 3(8):1799–1808. https://doi.org/10.1021/acsbiomaterials.7b00260
14. Zhu ZJ, Su M (2017) Polydopamine nanoparticles for combined chemo- and photothermal cancer therapy. Nanomaterials 7(7):160. https://doi.org/10.3390/nano7070160
15. Zou KY, Li ZX (2018) Controllable syntheses of MOF-derived materials. Chemistry 24(25):6506–6518. https://doi.org/10.1002/chem.201705415
16. Lynge ME, Van Der Westen R, Postma A et al (2011) Polydopamine—a nature-inspired polymer coating for biomedical science. Nanoscale 3(12):4916–4928. https://doi.org/10.1039/c1nr10969c
17. Chen S, Cheng AC, Wang MS et al (2008) Detection of apoptosis induced by new type gosling viral enteritis virus in vitro through fluorescein annexin V-FITC/PI double labeling. World J Gastroenterol 14(14):2174–2178. https://doi.org/10.3748/wjg.14.2174
18. Kim H, Xue X (2020) Detection of total reactive oxygen species in adherent cells by 2',7'-dichlorodihydrofluorescein diacetate staining. J Vis Exp 160:e60682. https://doi.org/10.3791/60682
19. Dingeldein A, Aden J, Sparrman T et al (2017) Mitochondrial membrane organization in regulation of apoptosis. Biophys J 112(3):224a. https://doi.org/10.1016/j.bpj.2016.11.1233
20. Sun YZ, Davis EW (2019) Facile fabrication of polydopamine nanotubes for combined chemo-photothermal therapy. J Mater Chem B 7(43):6828–6839. https://doi.org/10.1039/c9tb01338e
21. Dai LL, Li X, Duan XL et al (2019) A pH/ROS cascade-responsive charge-reversal nanosystem with self-amplified drug release for synergistic oxidation-chemotherapy. Adv Sci 6(4):1801807. https://doi.org/10.1002/advs.201801807
22. Lismont M, Dreesen L, Wuttke S (2017) Metal-organic framework nanoparticles in photodynamic therapy: current status and perspectives. Adv Funct Mater 27(14):1606314. https://doi.org/10.1002/adfm.201606314